Radio Frequency Fields in Multiple-Cavity Masers

J. Shell[1]

A computer program has been written to calculate the radio frequency (RF) electric and magnetic fields inside a cascaded network of rectangular waveguide junctions. It is based on a mode-matching program developed in JPL's Communications Ground Systems Section. This program has been used to calculate the stored energy in the cavities of the current 32-GHz multiple-cavity maser design, as well as the interaction between the RF magnetic field and the ruby spins at the signal and pump frequencies.

I. Introduction

The current 32-GHz multiple-cavity maser (MCM) design is a coupled-cavity arrangement of cascaded rectangular waveguide sections operating in a reflection mode [1]. Although it is a cavity design, the performance is similar to a traveling-wave maser because the frequency of operation may be adjusted by tuning the dc magnetic field strength and the microwave pump sources. In this way, the 31.8-GHz-to-32.3-GHz deep-space-to-Earth allocation may be covered. A rectangular waveguide mode-matching program was used to calculate the scattering parameters of various maser designs during the development work leading to the current 32-GHz MCM design [2]. This program was used to determine the frequency response of the coupled-cavity structure. The spin system losses were simulated by assigning suitable dielectric loss tangents to the ruby-filled cavity. The maser design was based on the scattering parameters obtained from the program.

The maser's performance actually depends upon the interaction between the quantum mechanical spin system in the active maser material and the RF magnetic field. The "spins" are the localized magnetic moments associated with the chromium ions in the ruby crystal. Knowledge of the RF magnetic field geometry in the cavities is needed to further optimize the design to maximize the maser performance. This knowledge and optimization is needed in the signal frequency range from 31.8 GHz to 32.3 GHz and in the pump frequency range between 65.9 GHz and 66.9 GHz. The same volume of ruby that interacts with the signal frequency RF magnetic field must also interact with the pump frequency RF magnetic field.

The mode-matching program does not normally provide information about the geometry of the RF electromagnetic fields inside the cavities. Therefore, an algorithm based on mode-matching was developed and is used to calculate RF electric and magnetic fields within the coupled-cavity maser structure. The algorithm to calculate the RF electric and magnetic fields within the coupled-cavity maser structure is described in this article, as are some results specific to the current 32-GHz MCM.

---

[1] Communications Ground Systems Section.

The research described in this publication was carried out by the Jet Propulsion Laboratory, California Institute of Technology, under a contract with the National Aeronautics and Space Administration.

II. Modal Expansion of the Fields

The waveguides comprising the maser can be thought of as transmission lines capable of supporting many modes, both propagating and evanescent. The electric and magnetic fields inside an arbitrary but uniform waveguide can be expanded in a series of the waveguide mode functions as [3]

$$\left.\begin{aligned} E(x,y,z) &= \sum_n v_n(z)E_{tn}(x,y) + i_n(z)E_{zn}(x,y) \\ H(x,y,z) &= \sum_n i_n(z)H_{tn}(x,y) + v_n(z)H_{zn}(x,y) \end{aligned}\right\} \tag{1}$$

where the $v_n(z)$ and $i_n(z)$ are a measure of the rms amplitudes of the transverse and longitudinal electric and magnetic fields. They also account for the field variation along the longitudinal direction z and satisfy transmission line equations of the form

$$\left.\begin{aligned} \frac{dv_n(z)}{dz} &= -j\kappa_n Z_o^{(n)} i_n(z) \\ \frac{di_n(z)}{dz} &= -j\kappa_n Y_o^{(n)} v_n(z) \end{aligned}\right\} \tag{2}$$

where $Z_o^{(n)}$ is the impedance of the nth mode and $\kappa_n = \sqrt{k^2 - k_{nc}^2}$. The E_{tn} and H_{tn} are the transverse components of the modal fields and are normalized in the sense that $|E_{tn}|^2$ and $|H_{tn}|^2$ integrated over the waveguide cross section are unity. The transverse electric (TE) modes are given by [3]

$$\left.\begin{aligned} E_{xn}(x,y) = H_{yn}(x,y) &= \frac{\sqrt{\varepsilon_m \varepsilon_n}}{b} \frac{n}{\sqrt{m^2\frac{b}{a} + n^2\frac{a}{b}}} \cos\left(\frac{m\pi x}{a}\right) \sin\left(\frac{n\pi y}{b}\right) \\ E_{yn}(x,y) = -H_{xn}(x,y) &= -\frac{\sqrt{\varepsilon_m \varepsilon_n}}{a} \frac{m}{\sqrt{m^2\frac{b}{a} + n^2\frac{a}{b}}} \sin\left(\frac{m\pi x}{a}\right) \cos\left(\frac{n\pi y}{b}\right) \end{aligned}\right\} \tag{3}$$

The longitudinal TE components of the field are given by

$$\left.\begin{aligned} E_{zn}(x,y) &= 0 \\ H_{zn}(x,y) &= -j\eta\lambda \frac{\sqrt{\varepsilon_m \varepsilon_n}}{2ab} \sqrt{m^2\frac{b}{a} + n^2\frac{a}{b}} \cos\left(\frac{m\pi x}{a}\right) \cos\left(\frac{n\pi y}{b}\right) \end{aligned}\right\} \tag{4}$$

In these expressions, a and b are the waveguide transverse dimensions, $\varepsilon_m = 1$ if the mode index $m = 0$ and $\varepsilon_m = 2$ if $m \neq 0$, η is the admittance of the medium, and λ is the wavelength in the medium. The boundary conditions along surfaces parallel to the direction of propagation, such as the waveguide side and top walls, are satisfied by the mode functions separately and, therefore, also by the sum. The mode amplitudes v_n and i_n are adjusted in magnitude and phase so that the boundary conditions along irises and apertures are satisfied. A similar set of equations exists for the transverse magnetic (TM) modes, but they are not needed if there is no variation in the y-direction and the incident mode is TE_{10}.

III. Connection Between the Modal Amplitudes and the Traveling-Wave Amplitudes

The mode-matching program is based on a scattering description of the fields. This means the solution to the wave equations, Eq. (2), are expressed as a superposition of exponential functions

$$\left.\begin{aligned} v_n(z) &= a_n(z')e^{-j\kappa_n(z-z')} + b_n(z')e^{j\kappa_n(z-z')} \\ Z_o^{(n)} i_n(z) &= a_n(z')e^{-j\kappa_n(z-z')} - b_n(z')e^{j\kappa_n(z-z')} \end{aligned}\right\} \tag{5}$$

where $a_n(z')$ and $b_n(z')$ are complex amplitudes representing the forward and backward traveling waves at $z = z'$. The output of the mode-matching program is the set of scattering parameters for all the modes used in the calculation. This means that each S-parameter, rather than being simply a complex number, is a matrix. For example, $S_{11}(p, q)$ is the reflection coefficient when the qth mode is incident and the pth mode is reflected. The pth and qth modes need not be propagating; they may be evanescent. This allows the discontinuities to be placed close together, and they may even interact.

From Eq. (5), we can see the connection between the mode amplitudes used in Eq. (1), $v_n(z)$ and $i_n(z)$, and the traveling-wave amplitudes, $a_n(z')$ and $b_n(z')$. The mode voltages and currents can be found by solving Eq. (5) for v_n and i_n at $z = z'$. Then,

$$\left.\begin{aligned} v_n &= a_n + b_n \\ i_n &= \frac{(a_n - b_n)}{Z_o^{(n)}} \end{aligned}\right\} \tag{6}$$

If we multiply both above equations by $\sqrt{Z_o^{(n)}}$ and redefine $v_n' = v_n\sqrt{Z_o^{(n)}}$ and $i_n' = i_n\sqrt{Z_o^{(n)}}$, we obtain

$$\left.\begin{aligned} v_n' &= (a_n + b_n)\sqrt{Z_o^{(n)}} \\ i_n' &= \frac{(a_n - b_n)}{\sqrt{Z_o^{(n)}}} \end{aligned}\right\} \tag{7}$$

This definition of the mode amplitudes implies a power flow down the waveguide for the nth mode of

$$P_n = \mathrm{Re}(v_n' i_n'^*) = a_n^* a_n - b_n^* b_n \tag{8}$$

that is consistent with the definition used by the mode matching program [2]. For the TE modes, the characteristic impedance is given by

$$Z_o^{(n)} = \frac{j\omega\mu}{\gamma_n} \tag{9}$$

where ω is the angular frequency, μ is the permeability, and γ_n is the propagation constant of the nth mode, given by

$$\gamma_n = \sqrt{\left(\frac{2\pi}{\lambda_{cn}}\right)^2 - \left(\frac{2\pi}{\lambda_o}\right)^2 \frac{\varepsilon}{\varepsilon_o}} \tag{10}$$

where λ_{cn} is the cut-off wavelength of the nth mode, given by

$$\lambda_{cn} = \frac{2\sqrt{ab}}{\sqrt{m^2\frac{b}{a} + n^2\frac{a}{b}}} \tag{11}$$

IV. Determination of the Traveling-Wave Amplitudes from the Generalized Scattering Parameters

Up to this point we have expressed the electric and magnetic fields in terms of a modal expansion, and we have related the mode amplitudes to the traveling-wave amplitudes in Eq. (7). The last step is to calculate the traveling-wave amplitudes at a given reference plane from the scattering parameters. This can be done in the following way. One half of the maser structure, up to and including part of the cavity of interest, is called network A, and the other half is called network B. See Fig. 1. The usual equations for S-parameters can be written

$$\left.\begin{aligned} b_1^A &= S_{11}^A a_1^A + S_{12}^A a_2^A \\ b_1^B &= S_{11}^B a_1^B + S_{12}^B a_2^B \\ b_2^A &= S_{21}^A a_1^A + S_{22}^A a_2^A \\ b_2^B &= S_{21}^B a_1^B + S_{22}^B a_2^B \end{aligned}\right\} \tag{12}$$

Imposing the continuity conditions that $b_2^A = a_2^B$ and $a_2^A = b_2^B$ leads to the following set of equations:

$$\left.\begin{aligned} b_1^A - S_{12}^A a_2^A &= S_{11}^A a_1^A \\ a_2^A - S_{22}^B b_2^A &= S_{21}^B a_1^B \\ b_2^A - S_{22}^A a_2^A &= S_{21}^A a_1^A \\ b_1^B - S_{12}^B b_2^A &= S_{11}^B a_1^B \end{aligned}\right\} \tag{13}$$

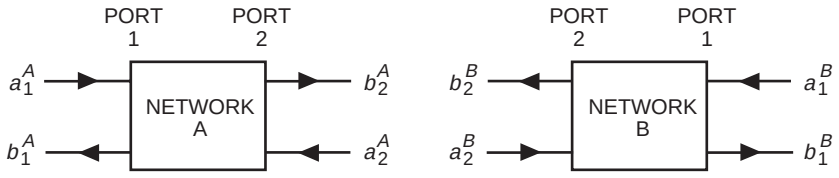

Fig. 1. The break up of the microwave structure into two parts and the traveling-wave amplitudes associated with each part.

This can be written in matrix form as

$$\begin{bmatrix} I_1 & 0 & -S_{12}^A & 0 \\ 0 & I_2 & -S_{22}^A & 0 \\ 0 & -S_{22}^B & I_3 & 0 \\ 0 & -S_{12}^B & 0 & I_4 \end{bmatrix} \begin{bmatrix} b_1^A \\ b_2^A \\ a_2^A \\ b_1^B \end{bmatrix} = \begin{bmatrix} S_{11}^A & 0 \\ S_{21}^A & 0 \\ 0 & S_{21}^B \\ 0 & S_{11}^B \end{bmatrix} \begin{bmatrix} a_1^A \\ a_1^B \end{bmatrix} \tag{14}$$

The computer program analyzes the networks A and B separately. It calculates the generalized S-matrices and forms the matrix equation above. Finally, it solves for a_2^A and b_2^A. Notice that a_2^A and b_2^A are vectors composed of the forward and backward traveling-wave amplitudes for all of the modes of interest. Using Eq. (7), the mode amplitudes are calculated, and using Eq. (1), the fields are calculated. This process is repeated for each desired transverse slice in the cavity of interest. The fields can be written to a separate file, which can be read by MATLAB [4] to make two-dimensional vector plots of the fields or three-dimensional plots of the stored energy or transition probabilities.

V. Energy Storage

If a sufficiently large number of slices is made through the cavity, and each slice is subdivided into a number of points, a two-dimensional grid of values of the electric and magnetic fields can be found. Since a_n and b_n are complex, so also are v_n and i_n. These resulting electric and magnetic fields are in phasor form, having real and imaginary components. The maximum value of the field is given by the complex absolute value of the phasor. The electric energy density and magnetic energy density are given by

$$U_E = \frac{1}{2}\varepsilon \left|E\right|^2 \tag{15a}$$

and

$$U_H = \frac{1}{2}\mu \left|H\right|^2 \tag{15b}$$

These are calculated at each point of the two-dimensional grid. Since the fields are uniform in the vertical direction, the total energy in the cavity is approximately the average value of the energy density over the grid times the volume of the cavity.

VI. Transition Probability

As mentioned previously, the quantum transitions in the ruby are induced by the RF magnetic field. The general expression for the transition probability between two quantum states j and k in a paramagnetic system is given by [5]

$$W_{jk} = \frac{1}{4}\gamma^2 g(f) \left|\mathbf{H}_{RF}^* \cdot \langle j \left|\mathbf{S}\right| k\rangle\right|^2 \tag{16}$$

In this expression, γ is the ratio of the magnetic moment to the angular momentum of the spin. (This γ should not be confused with the propagation constant defined earlier or the appearance in Table 1 for the directional transition probabilities.) The function $g(f)$ is called the line shape and determines how the transition probability behaves as one moves away from the resonant frequency. The quantity $\mathbf{S}$ is

a quantum mechanical operator describing the effective spin. The quantities $\langle j|$ and $|k\rangle$ are the vectors representing the quantum states j and k. The quantity $\langle j|\mathbf{S}|k\rangle$ is a dimensionless vector characteristic of the particular j–k transition and the strength of the dc magnetic field and its orientation relative to the c-axis of the ruby. Its calculation is a problem in quantum mechanics.[2] The vector components of $\langle j|\mathbf{S}|k\rangle$ are usually expressed in the form (α, β, γ). These values for ruby whose c-axis is 54.735 deg from the applied dc field and whose strength is 11.8 kG are shown in Table 1 for the quantum transitions of interest. In this article, we will not include $g(f)$, which is dependent on the dc magnetic field shape and the natural line width of the ruby. The constant factor $(1/4)\gamma^2$ will also be omitted.

Table 1. Components of $\langle j|\mathrm{S}|k\rangle$ for ruby with H_{dc} = 11.8 kG at 54.735 deg to the c-axis.

Quantum transition	α	β	γ
Level 2 ↔ 3	−1.96	0.087	j1.96
Level 1 ↔ 3	−0.291	−0.20	j0.304
Level 2 ↔ 4	−0.258	−0.20	j0.237
Average of (1 ↔ 3) + (2 ↔ 4)	−0.2745	−0.20	j0.2705

VII. Application to the Ka-Band Multiple-Cavity Maser

The geometry of the multiple-cavity maser is shown in Fig. 2. A calculation of the stored magnetic energy in the signal broadbanding cavity, the ruby cavity, and the pump broadbanding cavity as a function of frequency is shown in Fig. 3. It is interesting to note that at the center of the tuning range, near 32 GHz, very little energy is stored in the coupling cavity. As one moves away from 32 GHz in either direction, the energy stored in the coupling cavity increases, peaking at 31.5 and 32.65 GHz. This is an example of what Siegman [5] describes as frequency-dependent feedback. He explains it in the following way. Ignoring the reactive effects of the spin system, the coupling cavity and ruby cavity can be represented by the lumped circuit shown in Fig. 4. A signal exactly on resonance passes through the shunt circuit with no loss, is amplified by the ruby, and passes back out through the shunt circuit. A signal slightly off resonance is scattered slightly by the shunt circuit in traveling into the ruby cavity. More importantly, some of the amplified signal leaving the ruby cavity is scattered by the shunt circuit back into the ruby cavity for additional amplification.

A simple check of the field calculation program can be made in the following way. From very general principles, the frequency dependence of a lossless junction follows the relation [6]

$$-\frac{d\phi}{d\omega} = \frac{W}{P} \tag{17}$$

which states in words that the electrical line length into the termination and out again always increases with frequency, and the rate of increase is equal to the stored energy per unit incident power. The left-hand side of the equation can be calculated using the original mode-matching program. The right-hand

[2] R. W. Berwin, "Paramagnetic Energy Levels of the Ground State of Cr+3 in Al2O3 (Ruby)," JPL Technical Memorandum 33-440, Jet Propulsion Laboratory, Pasadena, California, January 15, 1970.

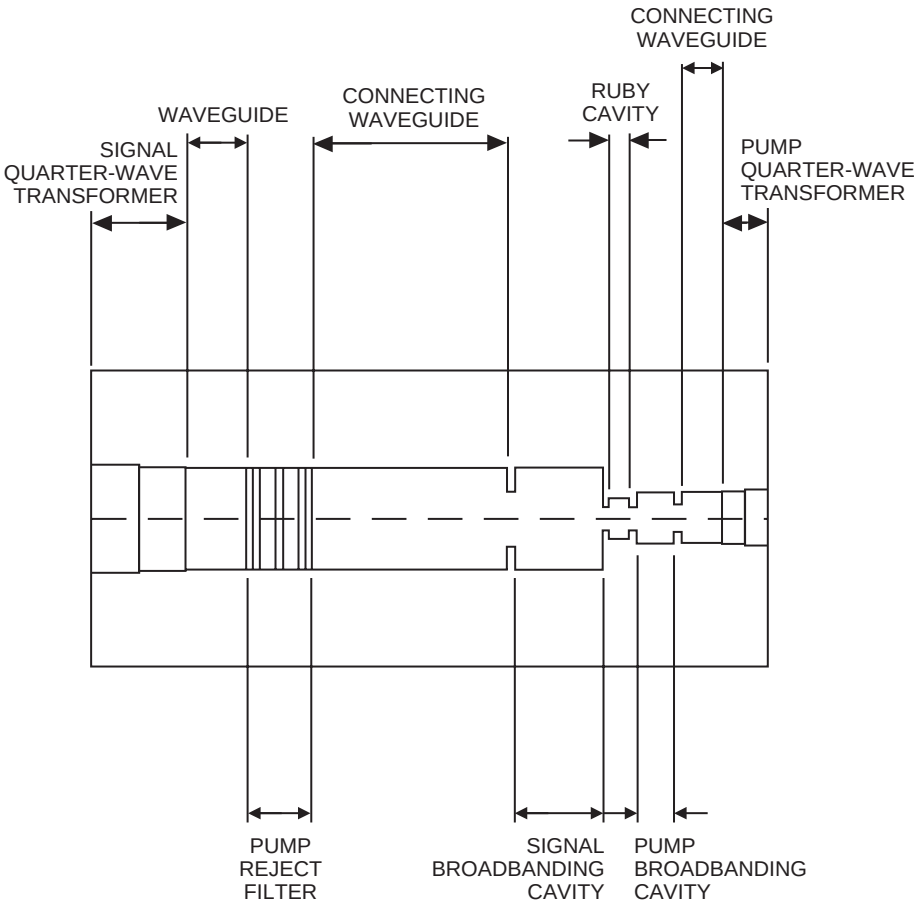

Fig. 2. Top view of the Ka-band multiple-cavity maser design (from [1]). The signal power is incident from the left; the pump power is incident from the right.

side of the equation can be calculated by summing the total electric and magnetic stored energy in all three cavities. The curves are shown in Fig. 5. The reader can see that the curves are in quite close agreement.

Another way to check the program is to estimate the stored electric energy in a given cavity by examining the dissipative loss using the original mode-matching program. A dissipative loss can be accounted for by including an imaginary component of the dielectric constant. An imaginary component of the dielectric constant is applied to each cavity in turn, and the reflection coefficient, S_{11}, for the complete structure is calculated. The quantity $(1 - S_{11}^2)$ is shown in Fig. 6. One can see that the shape of the curves for the dissipative loss in the ruby cavity and the coupling cavity closely matches the curves in Fig. 3. The total dissipative loss closely resembles the curves in Fig. 5. Calculation at the pump frequencies looking from the pump end of the structure gives a similar response.

In the coupled-cavity maser, the ruby cavity is resonant at the signal frequency. It is also resonant at the pump frequency in the presence of the signal broadbanding cavity and the pump reject filter. Tabulations of the quantity $TP = |\mathbf{H}_{RF}^* \cdot \langle j\,|\mathbf{S}|\,k\rangle|^2$ over a 45-by-45 grid inside the ruby crystal have been made. The curves in Fig. 7 include only the effects of the signal broadbanding cavity, ruby cavity, and pump broadbanding cavity. The quarter-wave transformers and pump reject filter should have no effect and are not included. Figure 7(a) shows a plot for this calculation at 32.0 GHz. The values for the directional transition probability are given in the first row of Table 1. The base of the plot corresponds to the base of the ruby crystal. In Fig. 2, it corresponds to the area labeled "ruby cavity." The height of the

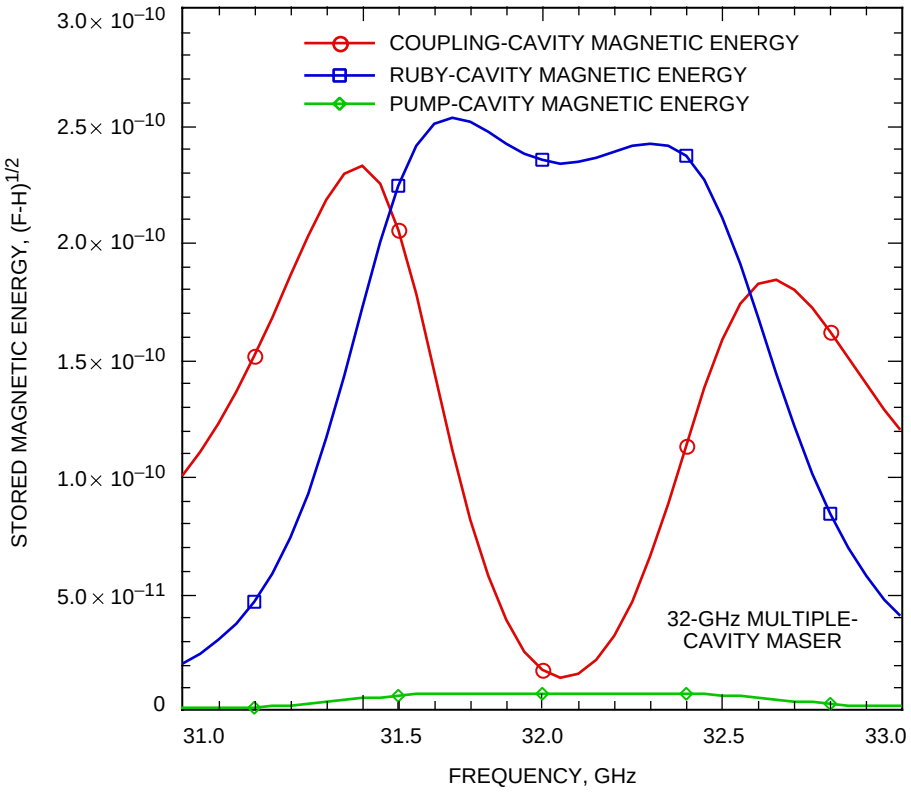

Fig. 3. The stored magnetic energy in the signal broadbanding cavity, ruby cavity, and pump broadbanding cavity versus frequency.

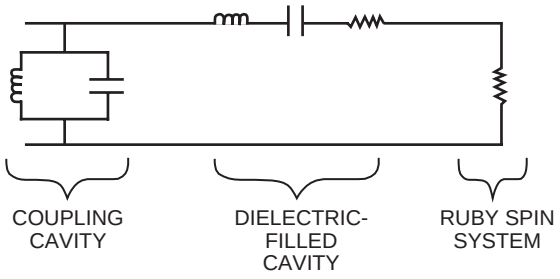

Fig. 4. Simplified lumped-element representation of the signal broadbanding cavity and ruby-filled cavity.

plot corresponds to the value of TP at that location. The same plot applies at any horizontal plane within the ruby crystal. The arrow on the figure indicates the view looking from the signal broadbanding cavity. The large transition probabilities near the edges of the inductive irises stand out. The interaction with the ruby spin system is very strong at these points. Figure 7(b) shows the same plot from a lower elevation angle and an expanded scale. The plot is characterized by the bowl-shaped depression in the center of the ruby. This is expected because the magnetic field is very weak in the center of a half-wavelength cavity. The interaction falls to zero at the corners of the ruby and rises to a local maximum half the distance of the cavity along the side walls. It also falls to a local minimum in the center of the apertures of the inductive irises. The value there is slightly greater than the local maximum at the side walls. The shape of this surface changes little over the frequency band from 31.8–32.3 GHz.

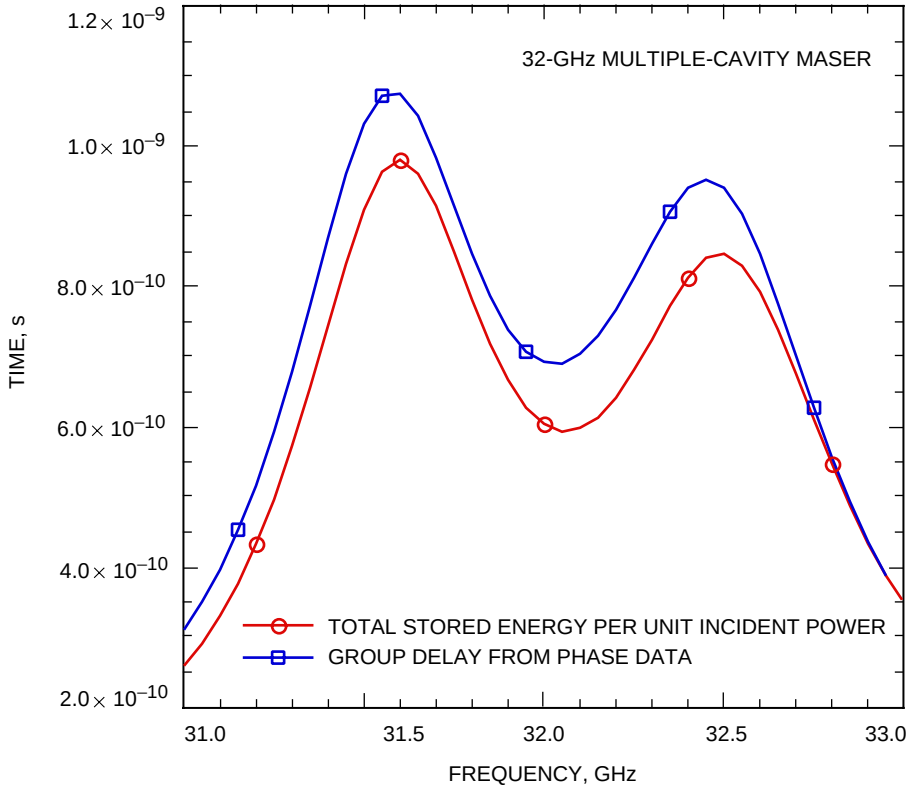

Fig. 5. The total stored energy (electric and magnetic) and group delay versus frequency.

Because the computer code has not been generalized to handle TM modes as of this writing, the pump reject filter was replaced with a waveguide beyond cutoff located 1.177 cm from the 3.6068-mm iris. A short circuit could not be used because no transmitted modes would be generated, and the algorithm described in Section III would fail. The directional transition probabilities used for this calculation are shown in Table 1 as the average values for the quantum transitions between levels 1 and 3 and levels 2 and 4. Figure 8(a) shows the quantity TP over a 45-by-45 grid in the ruby cavity at a pump frequency of 65.9 GHz. The viewpoint is the same as that used in Fig. 7(a). The interaction is again strong near the two side walls. However, it is also strong between the side wall and the center of the cavity, showing the clear presence of a TE_{301} mode. The presence of the TE_{102} mode is not very strong, as indicated by the weak interaction down the center line of the cavity. The interaction in the aperture is relatively weak compared with the interaction at the side walls, in contrast to the case mentioned earlier at 32 GHz. There is a peaking of TP near the walls forming the inductive irises, but it is not as pronounced as in Fig. 7(a). There is also a slight asymmetry along the direction of propagation with the two central maxima occurring closer to the signal-coupling cavity.

Figure 8(b) shows a similar plot at 66.4 GHz. The surface is more symmetrical with the four main peaks occurring near the center of the ruby. The peaks due to the inductive irises are more nearly equal. Figure 8(c) shows a similar plot at 66.9 GHz. Now the asymmetry has shifted slightly in the other direction. The two central maxima are now slightly closer to the pump broadbanding cavity. The interaction in the aperture of the pump-coupling cavity is greater than the interaction in the aperture of the signal-coupling cavity. The peaks due to the inductive irises are larger at the front than the back, just the reverse from the situation at 65.9 GHz. However, the basic structure of the interaction does not change significantly from 65.9–66.9 GHz.

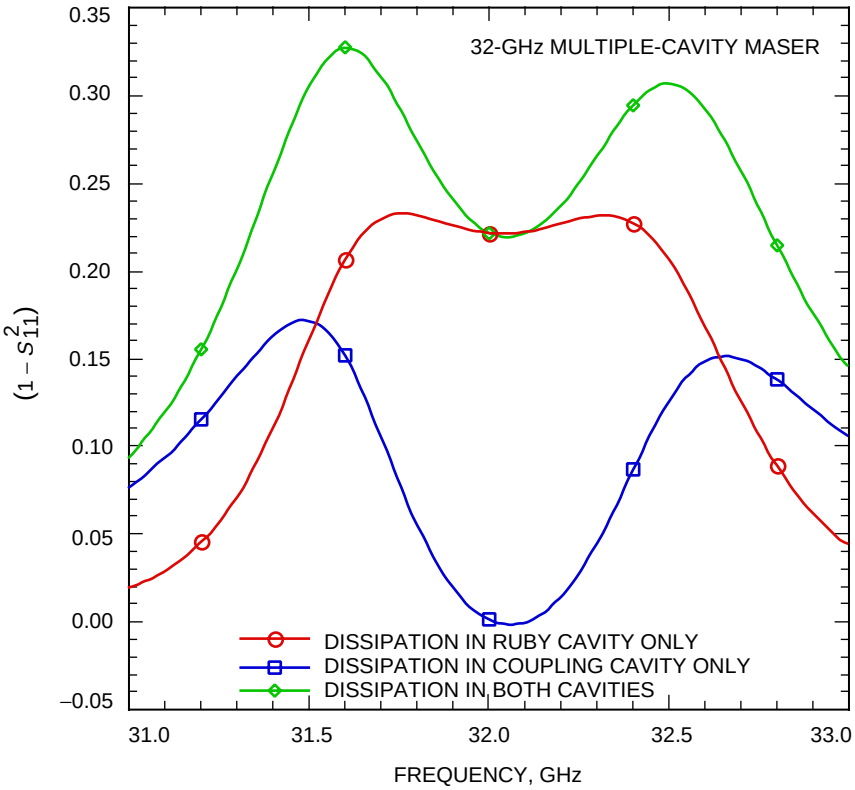

Fig. 6. The quantity $(1 - S_{11}^2)$ versus frequency for the ruby cavity, signal broadbanding cavity, and their sum.

The ability to make plots like these will enable future designers to better tailor the pump transition distribution to match the signal transition distribution. A different choice of iris dimensions may lead to greater excitation of the TE_{102} mode and less excitation of the TE_{301} mode. Different cavity dimensions that allow more pump modes to exist and the location of the pump reject filter can also be investigated. The further the filter is from the ruby cavity, the faster the pump transition distribution should change with frequency. This could be a factor in determining the effectiveness of the pump source frequency modulation.

In regards to accuracy, since the field components are calculated over a grid, the "integration" does not extend to the walls of the cavity. Thus, in calculating the stored field energy, the magnetic field, which is maximum near the walls, is slightly underestimated, and the electric field, which is zero at the walls, is slightly overestimated. As the grid becomes finer, the accuracy should improve. At this point, ohmic losses in the metal walls have not been included. The next version of the program may include these.

VIII. Conclusion

A computer program has been written to calculate the RF fields in a structure composed of cascaded sections of dielectric-filled rectangular waveguide. From the fields, the distribution of stored energy in the maser can be calculated. Using spin vector components for ruby, a quantity proportional to the transition probability between two quantum states can be calculated. The analysis is used to determine the coupling of the signal and pump RF magnetic fields to the ruby spins. This knowledge can be used with the scattering parameter data to optimize the dimensions of the ruby cavity, irises, and coupling cavities to improve the maser's performance.

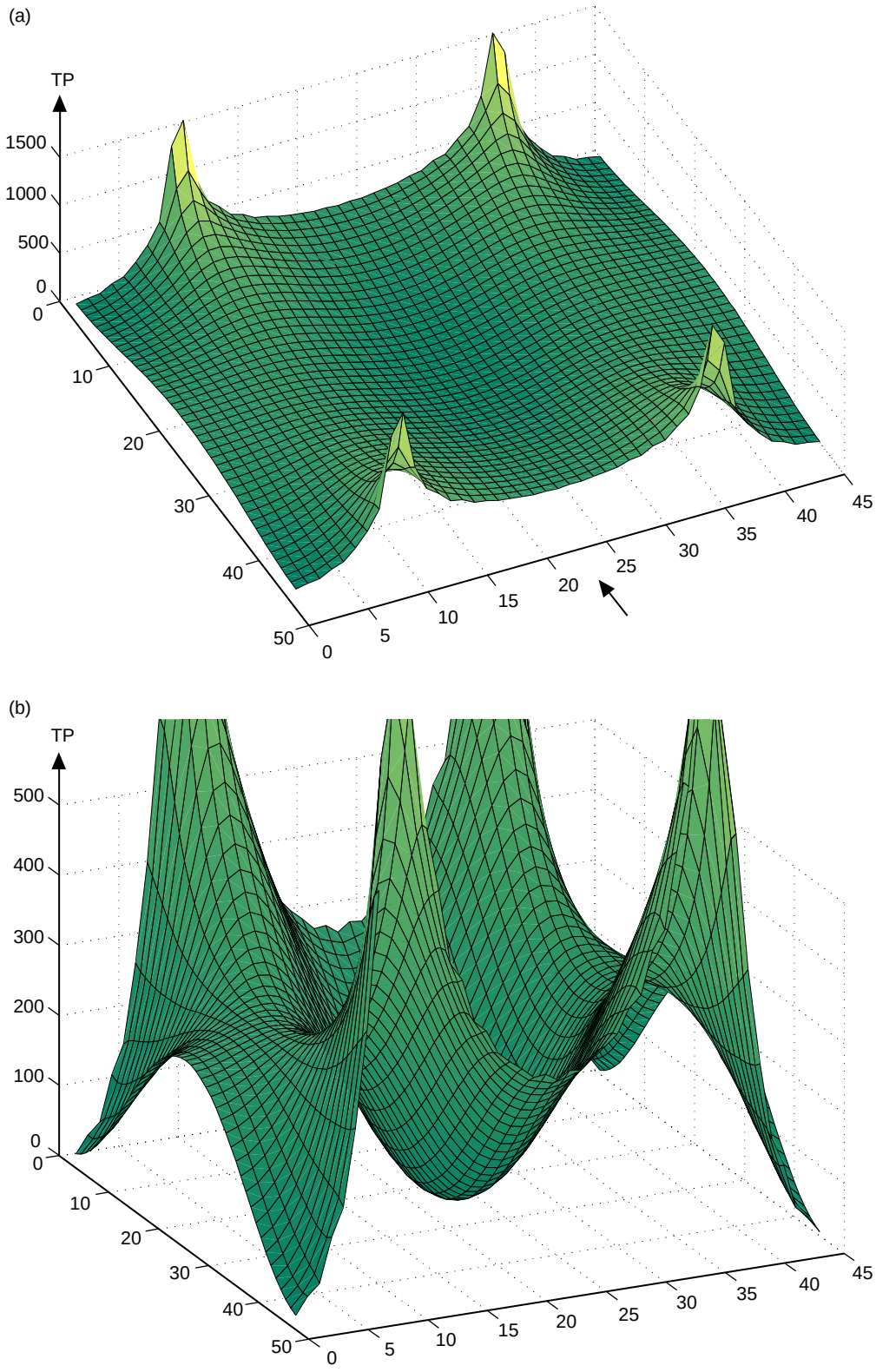

Fig. 7. TP versus location in the ruby crystal for any horizontal plane: (a) TP at 32 GHz and (b) the same as Fig. 7(a) but on an expanded scale and lower viewing angle.

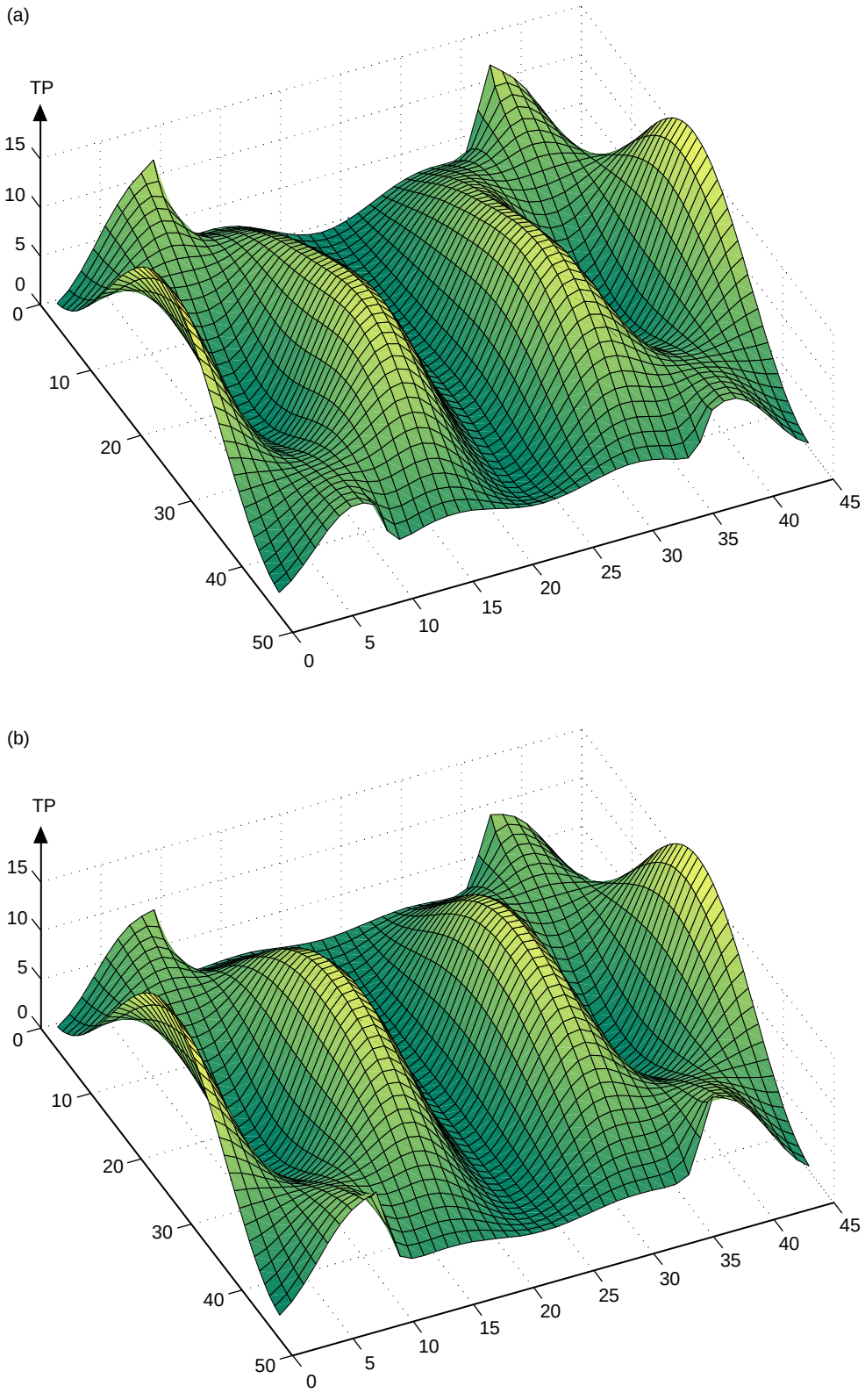

Fig. 8. TP versus location in the ruby crystal for any horizontal plane: (a) TP at 65.9 GHz, (b) TP at 66.4 GHz, and (c) TP at 66.9 GHz.

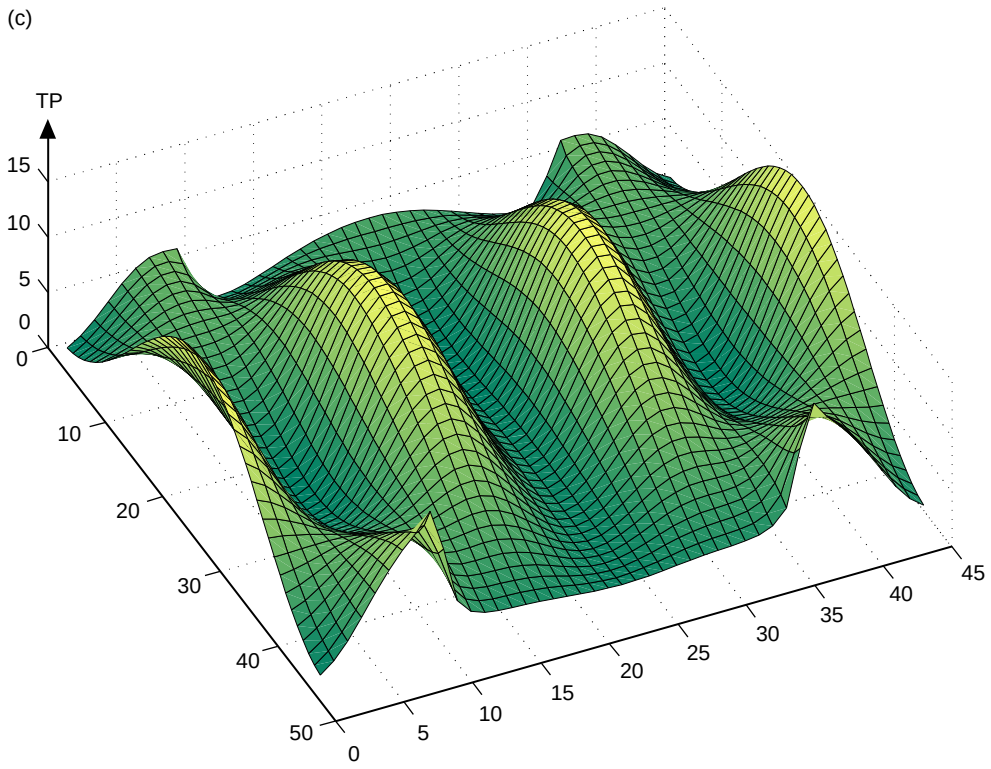

Fig. 8 (cont'd).

The program has yielded useful information for the relatively simple maser design discussed in this article. It can also be used for the 8400–8450 MHz (X-band) multiple-cavity maser currently under design or for more complex variations of the 32-GHz design mentioned in [1].

Acknowledgments

The author would like to thank Dr. Dan Hoppe for suggesting the algorithm on which this article is based. The author would also like to acknowledge useful discussions with Bob Clauss. He also suggested the use of the loss tangent of the dielectric constant as a way to estimate the stored energy in the electric field, and provided several useful test cases for the program.

References

[1] J. S. Shell and R. C. Clauss, "A 32-Gigahertz Coupled-Cavity Maser Design," *The Telecommunications and Mission Operations Progress Report 42-142, April–June 2000*, Jet Propulsion Laboratory, Pasadena, California, pp. 1–22, August 15, 2000.
http://tmo.jpl.nasa.gov/tmo/progress_report/42-142/142G.pdf

[2] D. J. Hoppe, "Modal Analysis Applied to Circular, Rectangular, and Coaxial Waveguides," *The Telecommunications and Data Acquisition Progress Report 42-95, July–September 1988*, Jet Propulsion Laboratory, Pasadena, California, pp. 89–96, November 15, 1988.
http://tmo.jpl.nasa.gov/tmo/progress_report/42-95/95I.PDF

[3] N. Marcuvitz, *Waveguide Handbook*, London: Peter Peregrinus Ltd., pp. 57,60, 1986.

[4] MATLAB, MathWorks, Inc., Natick, Massachusetts, copyright 1984–1998.

[5] A. E. Siegman, *Microwave Solid State Masers*, New York: McGraw-Hill Book Company, p. 178, 1964.

[6] C. G. Montgomery, R. H. Dicke, and E. M. Purcell, *Principles of Microwave Circuits*, New York: Dover Publications, Inc., p. 155, 1965.